Histopathology

CASE REPORT

Histopathology of Middle East respiratory syndrome coronovirus (MERS-CoV) infection – clinicopathological and ultrastructural study

Khaled O Alsaad,[1] [ID] Ali H Hajeer,[2,3] Mohammed Al Balwi,[2,4] Mohammed Al Moaiqel,[2,5] Nourah Al Oudah,[1,2] Abdulaziz Al Ajlan,[1,2] Sameera AlJohani,[2,6] Sami Alsolamy,[2,7] Giamal E Gmati,[2,8] Hanan Balkhy,[2,9] Hamdan H Al-Jahdali,[2,10] Salim A Baharoon[2,7] & Yaseen M Arabi[2,7]

[1]Division of Anatomical Pathology, Department of Pathology and Laboratory Medicine, King Abdulaziz Medical City, Riyadh, Saudi Arabia, [2]King Abdullah International Medical Research Center, Riyadh, Saudi Arabia, [3]Division of Immunopathology, Department of Pathology and Laboratory Medicine, King Abdulaziz Medical City, Riyadh, Saudi Arabia, [4]Division of Molecular Genetics and Cytogenetics, Department of Pathology and Laboratory Medicine, King Abdulaziz Medical City, Riyadh, Saudi Arabia, [5]Department of Medical Imaging, King Abdulaziz Medical City, Riyadh, Saudi Arabia, [6]Division of Microbiology, Department of Pathology and Laboratory Medicine, King Abdulaziz Medical City, Riyadh, Saudi Arabia, [7]Department of Intensive Care, King Abdulaziz Medical City, Riyadh, Saudi Arabia, [8]Division of Hematology, Department of Oncology, King Abdulaziz Medical City, Riyadh, Saudi Arabia, [9]Department of Infection Prevention and Control and Division of Infectious Diseases, Department of Pediatrics, King Abdulaziz Medical City, Riyadh, Saudi Arabia, and [10]Division of Pulmonology, Department of Medicine, King Abdulaziz Medical City, Riyadh, Saudi Arabia

Histopathology of Middle East respiratory syndrome coronovirus (MERS-CoV) infection – clinicopathological and ultrastructural study

Aims: The pathogenesis, viral localization and histopathological features of Middle East respiratory syndrome – coronavirus (MERS-CoV) in humans are not described sufficiently. The aims of this study were to explore and define the spectrum of histological and ultrastructural pathological changes affecting various organs in a patient with MERS-CoV infection and represent a base of MERS-CoV histopathology.

Methods and results: We analysed the post-mortem histopathological findings and investigated localisation of viral particles in the pulmonary and extrapulmonary tissue by transmission electron microscopic examination in a 33-year-old male patient of T cell lymphoma, who acquired MERS-CoV infection. Tissue needle biopsies were obtained from brain, heart, lung, liver, kidney and skeletal muscle. All samples were collected within 45 min from death to reduce tissue decomposition and artefact. Histopathological examination showed necrotising pneumonia, pulmonary diffuse alveolar damage, acute kidney injury, portal and lobular hepatitis and myositis with muscle atrophic changes. The brain and heart were histologically unremarkable. Ultrastructurally, viral particles were localised in the pneumocytes, pulmonary macrophages, renal proximal tubular epithelial cells and macrophages infiltrating the skeletal muscles.

Conclusion: The results highlight the pulmonary and extrapulmonary pathological changes of MERS-CoV infection and provide the first evidence of the viral presence in human renal tissue, which suggests tissue trophism for MERS-CoV in kidney.

Address for correspondence: Professor Yaseen M. Arabi MD, FCCP, FCCM, Chairman, Intensive Care Department, MC-1425, Medical Director, Respiratory Services, College of Medicine, King Saud bin Abdulaziz University for Health Sciences, King Abdullah International Research Center, PO Box 22490 Riyadh, 11426, Saudi Arabia. e-mail: arabi@ngha.med.sa; icu1@ngha.med.sa

Introduction

Middle East respiratory syndrome coronavirus (MERS-CoV) was first isolated from a patient who died from respiratory and renal failure in Saudi Arabia.[1,2] As of 14 July 2017, the World Health Organisation (WHO) was notified of 2040 global laboratory-confirmed cases of infection with MERS-CoV from 27 countries, 712 of which resulted in death.[3] MERS-CoV infection can be asymptomatic or cause disease that range from transient, self-limited common cold to severe acute hypoxaemic respiratory failure with a high case fatality rate.[4] Extrapulmonary organ dysfunction occurs commonly in MERS-CoV patients, particularly acute renal failure (ARF), which was reported to develop in 75% of critically ill patients.[5,6] Very limited histopathological data on human tissue, focusing primarily only on pathological changes in the lung, are available.[7] Furthermore, to date, no extrapulmonary morphological presence of MERS-CoV has been documented in humans. We present herein a description of histopathological changes and ultrastructural findings in a patient with MERS-CoV infection and, for the first time to our knowledge, describe and document the localisation of MERS-CoV in extrapulmonary locations.

CLINICAL HISTORY

A 33-year-old male was diagnosed with primary cutaneous T cell lymphoma on the scalp, face, trunk and upper and lower limbs in June 2014 and treated with chemotherapy followed by radiation. He was referred to King Abdulaziz Medical City, Riyadh on 18 May 2015 for further chemotherapy and possible stem cell transplant. Because the disease was not in complete remission, he received several lines of chemotherapy until July. On 29 July 2015 (hospital day 1), the patient presented to the emergency department with cellulitis and sepsis and was admitted for intravenous antibiotics therapy. On hospital day 12, he was given the SMILE protocol (methtrexate, ifosfamide, etoposide, L-asparginase and prednisolone). He developed thrombocytopaenia (the nadir platelet count was 2000 per cubic millimetre) and neutropaenia (absolute neutrophil count of 160 per cubic millimetre). The subsequent cycles of chemotherapy were held. On hospital day 21, he developed fever and productive cough with new infiltrate on chest radiograph (Figure 1) and was treated as healthcare-associated pneumonia. Sputum culture on hospital day 23 showed *Klebsiella pneumoniae* and *Acinetobacter baumannii*; MERS-CoV sputum real-time reverse transcription–polymerase chain reaction (rRT–PCR) was negative. On hospital day 42, repeated sputum MERS-CoV rRT–PCR was positive. On hospital day 43, he was admitted to the intensive care unit (ICU) because of increasing hypoxaemia and subsequently on hospital day 46 was intubated and ventilated mechanically. Chest radiograph showed bilateral infiltrates (Figure 1). He was managed with lung-protective ventilation strategy and neuromuscular blockade. Repeated MERS-CoV rRT–PCR from tracheal aspirates remained positive until his death. Kidney function tests showed mild impairment with peak serum creatinine of 154 µmol/l. Liver enzymes and creatine phosphokinase remained within normal range throughout the ICU stay. On hospital day 50, he died because of refractory shock and severe hypoxaemia. Throughout his ICU stay, he did not receive steroids, ribavirin or interferon.

Materials and methods

TISSUE COLLECTION

The Institutional Review Board of King Abdulaziz Medical City approved the study (protocol no. RC15/113/R – 1 September 2015). Informed consent was obtained from the patient's family. Under a complete aseptic technique using 2% chlorhexidine (chloraPrep with tent; CareFusion, El Paso, TX, USA) and full draping, a 14-gauge (G) needle (Max Core; Bard Peripheral Vascular, Tempe, AZ, USA) was used for tissue sampling. Multiple passes through the right lung, left ventricle of the heart, right hepatic lobe, right kidney and right anterior thigh skeletal muscles (SM) were performed. Additional multiple biopsies also were obtained from the right side of the brain
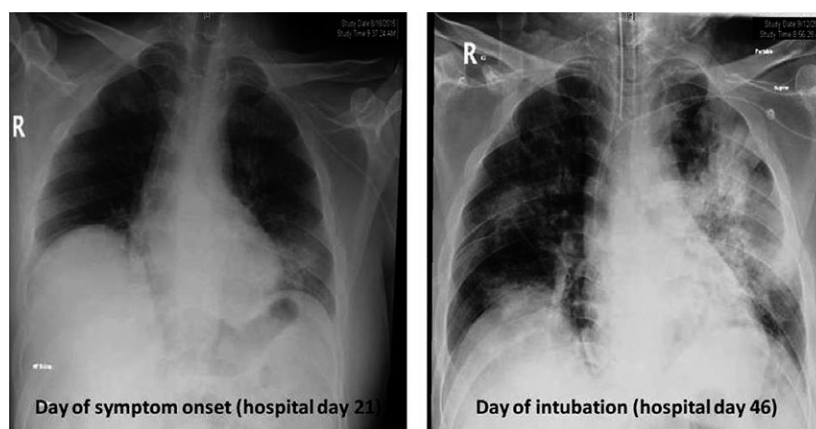
Figure 1. Chest radiographs at the time of symptoms of the Middle East respiratory syndrome coronavirus and at the time of intubation showing progressive deterioration of bilateral pulmonary infiltrates.

hemisphere using a Max Core needle after creating bone tract using an 11G bone injection needle bevelled tip (Tecres SPA, Verona, Italy). Full autopsy (evisceration) was not performed. Tissue samples were collected within 45 min from death to reduce the post-mortem decomposition and artefact, and all tissue biopsies except those from the brain were performed under ultrasound guidance.

TISSUE PROCESSING, SPECIAL STAINS AND IMMUNOHISTOCHEMISTRY

Tissue samples were fixed in 10% buffered formalin for 48 h, paraffin-embedded, sectioned at 5 μm (except for renal tissue, which was sectioned at 2 μm), mounted on glass slides and stained by routine haematoxylin and eosin (H&E). Using standard histochemical methods, Masson's trichrome (MT), periodic acid-Schiff (PAS), Grocott's methenamine special (GMS), Gram and Ziehl–Nelseen (ZN) special stains were performed on lung tissue. A renal panel that included PAS, Jones' methenamine silver and MT was also performed on renal tissue, and PAS, PAS with diastase, MT and reticulin special stains were performed on liver tissue. Immunostaining for histiocytic marker CD68 and lymphoid cell markers CD45, CD3, CD4 and CD8 were performed. Lung tissue was stained for cytomegalovirus (CMV). All immunoassays were performed according to the manufacturer's guidelines, using automated platform (Ventana Benchmark XT, Tucson, AZ, USA), and heat antigen retrieval by ultracell condition solution pH 8.4. The ultraview universal diaminobenzidine (DAB) detection kit was used for reaction visualisation. Correct positive and negative controls were utilised for histochemical and immunohistochemical (IHC) stains. Unfortunately, immunohistochemical work-up using anti MERS-CoV antibody to detect viral antigen in

Table 1. primary antibodies used for IHC, their clone, dilution and source

Antibody	Clone	Dilution	Source*
CD45	2B11 + PD7/26	1/200	Dako
CD3	Polyclonal	1/300	Dako
CD4	4B12	1/20	Dako
CD8	08/144b	1/25	Dako
CD68	KP1	1/50	Dako
CMV	CCH2/DDG9	1/50	Dako

IHC, immunohistochemistry.
*Dako, Denmark; Novus Biologicals; Littleton, CO, USA.

tissue was not performed. Table 1 summarises the IHC studies performed.

ELECTRON MICROSCOPY (EM)

Samples for ultrastructural study were fixed in 6% glutaraldehyde fixative prepared in sodium phosphate buffer (7.4 pH) for 4 weeks and underwent post-fixation in 1% osmium tetra-oxide for 1 h. The samples were washed twice by sodium phosphate buffer (7.4 pH) and dehydrated using increasing concentrations of acetone. The samples were then embedded in Araldite 520 resin and polymerised in an oven at 90°C for 48 and 24 h. Tissue semithin sections (1 μm) were prepared, stained by toluidine blue stain for 5 min and inspected under conventional light microscope. Ultrathin sections (70 nm) were prepared using a Leica EM UC7 ultramicrotome, collected on a 200-mesh copper grid (PELCO®) and stained with uranyl acetate for 15 min and lead citrate for 5 min. The stained ultrathin sections were screened by 120-

kV JOEL1230 transmission electron microscope (TEM) (Akishima, Tokyo, Japan) and images were obtained using a side-mounted digital camera (Gatan 780AJ03FA; Gatan, Inc., Pleasanton, CA, USA).

Results

LIGHT MICROSCOPY, HISTOCHEMICAL AND IHC FINDINGS

All tissue samples were well preserved and showed no autolysis. All samples examined showed no evidence of malignant lymphoproliferative disease or direct tissue damage by T cell lymphoma. No distinct viral inclusions were apparent in all organs by light microscopy (LM). Histopathological examination of lung tissue demonstrated severe acute haemorrhagic pneumonia and exudative diffuse alveolar damage (DAD). The histopathological changes were heterogeneous in severity. In the less affected areas, the lung parenchymal architecture was maintained and the alveolar spaces and interstitium contained variable numbers of pigmented pulmonary macrophages and scattered mononuclear inflammatory cells. Variable amounts of filamentous fibrin deposits were seen, mainly in the alveolar spaces (Figure 2A). In severely affected areas, the alveolar spaces were disrupted, ectatic and contained a large amount of blood and fibrin, mixed inflammatory cell infiltrate and cellular debris (Figure 2B). Pneumocyte hyperplasia and reactive changes, denudation and sloughing of alveolar cells, rare multinucleated syncytial cells, congestion of the alveolar walls and hyaline membrane formation were evident (Figure 2C). Areas of confluent parenchymal necrosis were seen (Figure 2D). Focal peri-bronchiolar acute and chronic inflammatory cell infiltrate was seen. No granulomas were identified. Focal subendothelial lymphocytic inflammatory infiltrate of lung interstitial vasculature was identified (Figure 2E).

PAS and GMS stains were negative for fungal elements, and Gram and ZN stains showed no evidence of bacterial and mycobacterial organisms, respectively. Immunostaining for CMV was negative. Immunoprofiling of the inflammatory response demonstrated the numerous intra-alveolar macrophages and infiltrating CD3^{+}, CD4^{+} and CD8^{+} T lymphocytes (Figure 2F) in the lung parenchyma. The subendothelial lymphocytes were predominantly CD4^{+} (Figure 2G).

The kidney showed features of tubular epithelial cell degenerative and regenerative changes/acute kidney injury (AKI) that included ectatic change of the renal tubules, uneven distribution of the tubular epithelial cells nuclei, nuclear hyperchromasia, necrosis, sloughing and loss of brush surface of the proximal tubular epithelial cells (PTEC) and mitotic activity (Figure 3A). The glomeruli appeared within normal size and showed mild ischaemic changes (Figure 3B). No endocapillary hypercellularity, subendothelial deposits, fibrinoid necrosis/karyorrhexis, crescent formation or microthrombi were seen. No interstitial inflammation was noted, and there was no interstitial fibrosis or tubular atrophy. No endarteritis-like lesion or vasculitis was identified. Immunohistochemically, no interstitial inflammation was noted.

The liver showed mild chronic lymphocytic portal inflammation (Figure 4A). No interface hepatitis or interlobular bile duct inflammation (ductitis)/damage were noted. The hepatic parenchyma appeared reactive and showed mild cellular hydropic degeneration (mainly in the perivenular areas), rare multinucleated hepatocytes and mild disarray of the hepatic plates. Mild sinusoidal lymphocytosis and small necroinflammatory foci were seen in the hepatic lobules. No portal or lobular granulomas were noted. Minimal macrovesicular perivenular steatotic change, sinusoidal congestion, haemorrhage and focal perivenular (zone 3) loss of hepatocytes were present (Figure 4B). By IHC studies, both CD4^{+} and CD8^{+} T lymphocytes were seen in the portal inflammatory infiltrate.

Histopathological examination of SM showed scattered angulated myofibres with variable degrees of atrophic changes. These were associated with mild myopathic changes, including fibre regeneration, internalised nuclei and fibre splitting (Figure 5A). Lymphohistiocytic inflammatory cell infiltrate was seen in the perimysium and endomysium (Figure 5A, inset). These inflammatory cells were CD68^{+}, CD3^{+}, CD4^{+} and CD8^{+} and more abundant in the areas of atrophic myofibres (Figure 5B). The brain and heart were unremarkable, and showed no significant inflammatory infiltrate.

EM FINDINGS

EM demonstrated viral particles (VP) in the cytoplasm of pneumocytes (Figure 6A) and alveolar macrophages (Figure 6B), renal PTEC (Figure 6C) and macrophages infiltrating the SM (Figure 6D,E). The VP presented singly or in small groups, and varied in size between 70 and 105 nm. Most VP were adjacent to the nuclear membranes and exhibited a dense round viral envelope and a surface decorated with electron-dense spike-like structures (Figure 6E,F). Meticulous examination failed to demonstrate VP in
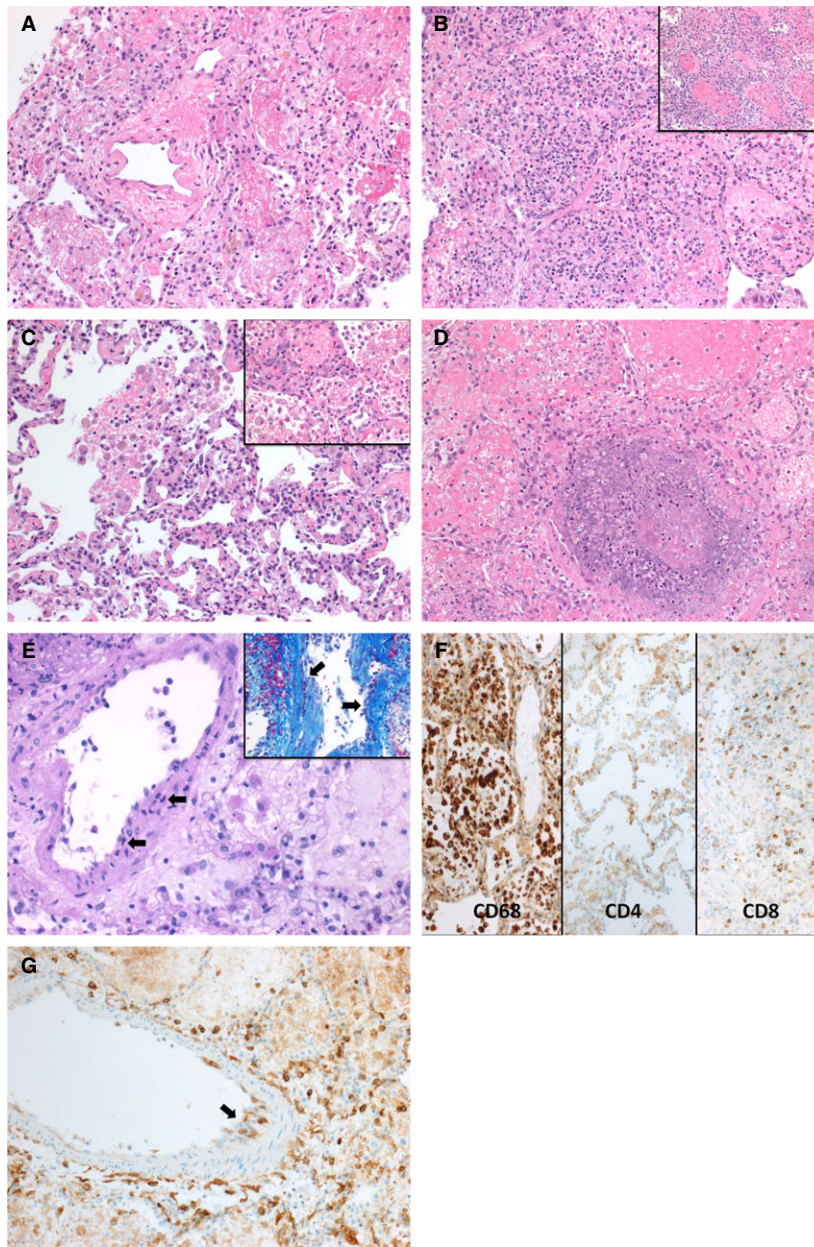
Figure 2. Pathological findings in the lung: **A**, Alveolar fibrin deposits, and alveolar and interstitial inflammation in less severely affected lung tissue [haematoxylin and eosin (H&E)]. **B**, Exuberant mixed inflammatory cell infiltrate, cellular debris, haemorrhage and fibrin deposition (inset) in ectatic and disrupted alveolar spaces in severely affected pulmonary tissue (H&E). **C**, Diffuse alveolar damage and formation of hyaline membrane (H&E, inset). **D**, Extensive pulmonary tissue necrosis (H&E). **E**, Subendothelial lymphocytic inflammatory infiltrate in interstitial arteries (intimal arteritis) (arrows) (H&E). **F**, Immunoprofiling of the pulmonary inflammatory infiltrate showing CD68+ macrophages and CD4+ and CD8+ lymphocytes (anti-CD68, CD4 and CD8). **G**, CD4+ lymphocytes infiltrating the subendothelial lining of the pulmonary interstitial vasculature (arrow) (anti-CD4).

glomerular epithelial cells, liver, heart and brain. In addition, no VP were identified in lymphocytes or endothelial cells in all examined organs. The histopathological, IHC and EM findings are summarised in Table 2.

Discussion

This report provides a detailed description of the histopathological changes and ultrastructural findings of a fatal case of MERS-CoV infection, and is the first report of the presence of MERS-Cov in organs other than the lung. The histopathological findings in the lung consisted of haemorrhagic necrotising pneumonia and exudative DAD with heterogeneous severity. These changes are similar to those described in animal model by de Wit *et al.*[8] and recently in humans by Ng *et al.*[7] An interesting morphological finding was the presence of CD4+ lymphocytic intimal arteritis, indicating an active immune response to injurious stimulus. This vascular injury was focal and not associated with intimal fibrinoid necrosis or thrombus
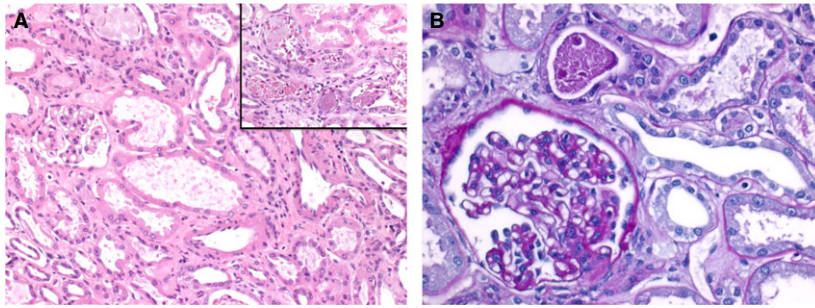
Figure 3. Pathological findings in the kidney: **A**, ectatic renal tubules and sloughed tubular epithelial cells in acute kidney injury (inset) (haematoxylin and eosin, inset). **B**, Mild ischaemic glomerular changes (periodic acid-Schiff).
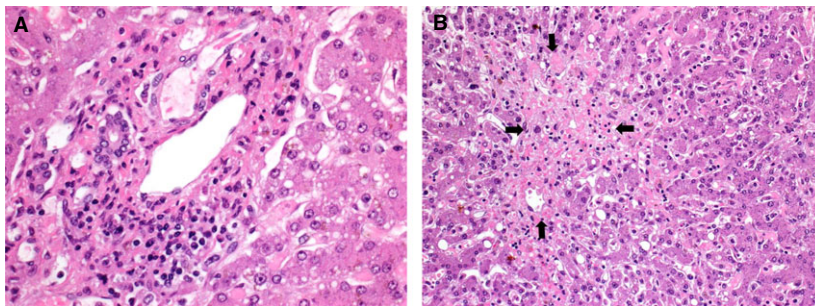
Figure 4. Pathological findings in the liver: **A**, mild chronic lymphocytic portal inflammatory cell infiltrate [haematoxylin and eosin (H&E)]. **B**, Perivenular necroinflammation and loss of hepatocytes (H&E).
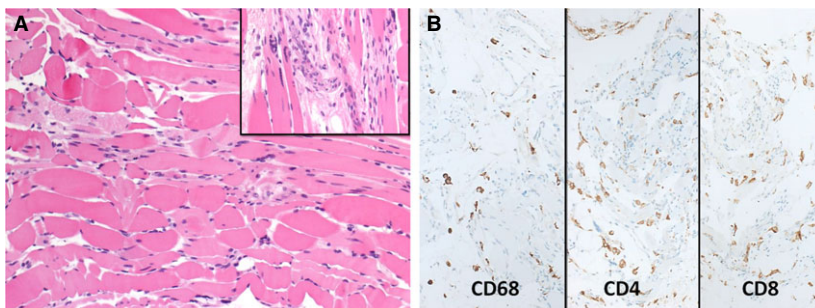
Figure 5. Pathological findings in skeletal muscles: **A**, atrophic and myopathic myofibre changes in the form of internalisation of the skeletal muscle nuclei, splitting of the muscle fibres and lymphohistiocytic inflammatory infiltrate (inset) (haematoxylin and eosin, inset). **B**, Immunoprofiling of inflammatory infiltrate showing CD68+ macrophages and CD4+ and CD8+ lymphocytes; the numbers of inflammatory cells were more abundant in atrophic myofibres (anti-CD68, CD4 and CD).

formation. Dipeptidylpeptidase 4 (DPP4)/CD26 is a recently described receptor, by which MERS-CoV enters target cells, and expressed in several types of cells including pneumocytes, renal tubular epithelial cells and endothelial cells.[6,9] Pulmonary microvascular thrombosis was described in lethal MERS-CoV in mice transgenic to human DPP4.[10] The presence of more aggressive vascular insult and thrombotic event, probably contributing to the necrotising nature

of lung disease, could not be excluded in our case. It is worth mentioning that during the clinical course, the patient had bacterial pneumonia which might have contributed to the pulmonary pathological findings at the time of post-mortem examination. Another intriguing finding in examined lung tissue was the ultrastructural localisation of the VP not only in the pneumocytes, as described previously,[7] but also in the alveolar macrophages.
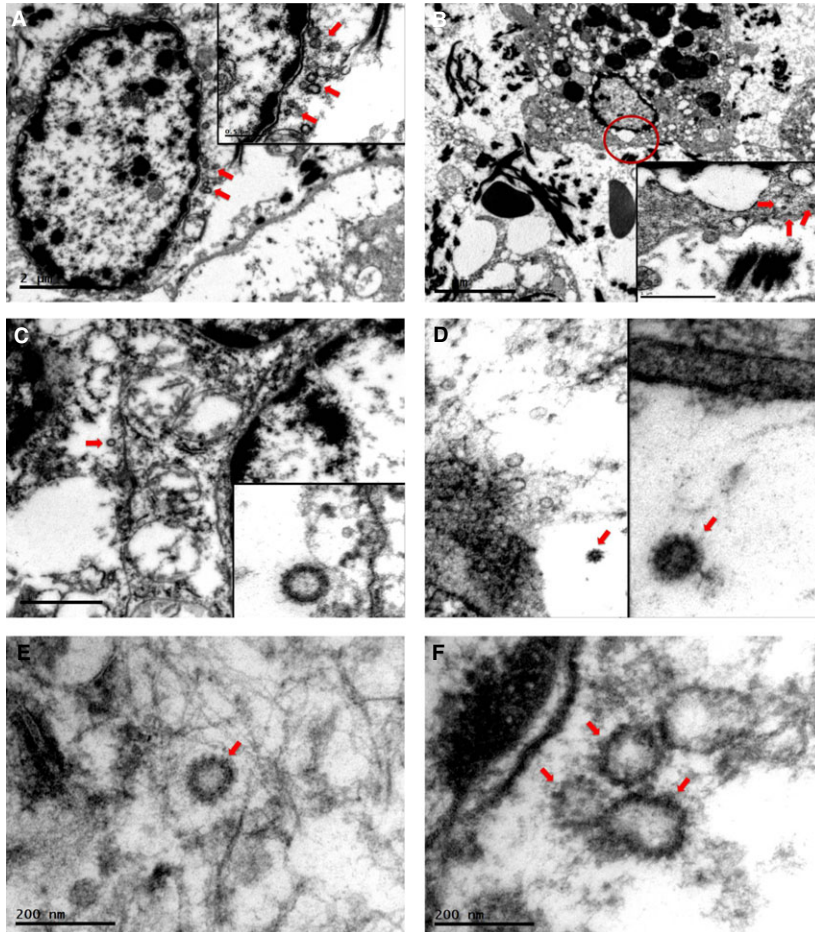
Figure 6. Ultrastructural findings: Middle East respiratory syndrome – coronavirus (MERS-CoV) particles were identified near the nuclear membrane and cytoplasm of **A**, pneumocytes (arrow), **B**, pulmonary macrophages (arrows), **C**, proximal renal tubular epithelial cells (arrow) and **D**, macrophages infiltrating smooth muscle (arrows). The viral particles presented singly **E**, VP in renal tubular epithelia cells or in small groups **F**, VP in pneumocytyes, exhibited electron-dense spike-like projections on the surface (arrows) (**E**,**F**) and ranged in size between 70 and 105 nm.

In *ex-vivo* models, the kidney epithelial cells were highly permissive for MERS-CoV replication and produced almost 1000-fold more infectious MERS-CoV progeny than bronchial epithelial cells.[6] In humans, MERS-CoV RNA was detected in urine samples.[11] Early and rapid-onset ARF is encountered commonly in patients with MERS-CoV infection, affecting the outcome of the disease negatively.[5,6,11,12] Recently, Yeung *et al.*[13] demonstrated disseminated MERS-CoV infection to the kidneys and other organs in an infected animal model. The presence of AKI in our patient is consistent with the recently published data on renal biopsy from a patient with MERS-CoV infection.[14] This is the first report, to our knowledge, of the presence of VP in renal PTEC. This finding supports the viral kidney trophism as a contributory factor in the pathogenesis of ARF in MERS-CoV infection. Surprisingly, despite the presence of VP in renal PTEC, no evidence of concurrent tubulointerstitial nephritis was identified.

Ultrastructural identifying of VP in macrophages infiltrating SM was the most exciting pathological and unexpected finding in this case. Myopathy in the form of focal myofibre necrosis, macrophagic infiltrate and regenerative changes were described in patients with severe acute respiratory syndrome coronavirus (SARS-CoV).[15] Although RT–PCR on SM was positive in a few cases, neither viral antigen nor VP could be identified, and SARS-CoV could not be isolated from SM tissue.[15–17] Whether the myopathic changes in our patient were a direct result of viral infection, immune-mediated or secondary to prolonged immobilisation could not be certain. However, detection of VP in the infiltrating macrophages in SM raises the possibility of viral trophism.

The mild portal and lobular hepatitis and hepatocellular reactive changes in our case are similar to those described in patients with SARS-CoV infection;[18] these changes are not specific and cannot be attributed in certainty to MERS-CoV infection. The perivenular congestion, haemorrhage and loss of hepatocytes in our patient can be attributed to impaired hepatic venous outflow.

Table 2. Light microscopic, immunohistochemical and ultrastructural findings of MERS-CoV infection

Organ	LM	IHC	VP localisation by EM
Lung	DAD, interstitial and alveolar acute and chronic inflammation, haemorrhagic NP, focal intimal arteritis	CD68^{+} macrophages and CD3^{+}/CD4^{+}/CD8^{+} lymphocytes in interstitium, alveolar walls and spaces; focal, predominantly CD4^{+} lymphocytic intimal arteritis	Pneumocytes and pulmonary macrophages†
Kidney	AKI, mild glomerular ischemic changes	No significant inflammatory cell infiltrate	PTEC†
Skeletal muscle	Atrophic changes, regenerative changes and myositis	CD68^{+} macrophages and CD3^{+}/CD4^{+}/CD8^{+} lymphocytes in perimysium and endomysium (atrophic myofibres > non-atrophic myofibres)	Infiltrating macrophages†
Liver	Mild lymphocytic chronic portal inflammation, mild lobular reactive changes and sinusoidal lymphocytosis, perivenular congestion, haemorrhage and loss of hepatocytes	CD3^{+}/CD4^{+}/CD8^{+} lymphocytes in portal tracts and sinusoidal spaces	Not identified
Brian and heart	Unremarkable	No significant inflammatory cell infiltrate	Not identified

LM, light microscopy; IHC, immunohistochemistry; VP, viral particles; EM, electron microscopy; DAD, diffuse alveolar damage; NP, necrotizing pneumonitis; AKI, acute kidney injury; PTEC, proximal tubular epithelial cells; MERS-CoV, Middle East respiratory syndrome – coronavirus.
†Cytoplasmic.

The mechanisms of viral deamination in MERS-CoV infection are not yet clear. Although VP were detected in pulmonary macrophages and macrophages infiltrating the SM, meticulous ultrastructural examination failed to demonstrate VP in lymphocytes, endothelial cells or lymphovascular channels. It is possible that our patient's reaction to MERS-CoV infection was atypical, owing to his immunosuppressive status due to his primary disease (lymphoma) and chemotherapy. Further detailed histological studies are needed to explore the morphological changes associated with MERS-CoV infection, and ultrastructural as well as immunohistochemical localisation studies are required to further enhance our understanding to viral pathogenesis.

In summary, we describe the pathological features and for the first time document the extrapulmonary tissue viral distribution in a fatal case of human MERS-CoV infection. Our findings provide insights into the morphological changes, pathogenesis and viral distribution of MERS-CoV.

Conflicts of interest

The authors declare no conflicts of interest.

References

1. Balkhy HH, Alenazi TH, Alshamrani MM, *et al.* Description of a hospital outbreak of Middle East respiratory syndrome in a large tertiary care hospital in Saudi Arabia. *Infect. Control Hosp. Epidemiol.* 2016; **37**; 1147–1155.
2. Zaki AM, van Boheemen S, Bestebroer TM, *et al.* Isolation of a novel coronavirus from a man with pneumonia in Saudi Arabia. *N. Engl. J. Med.* 2012; **367**; 1814–1820.
3. World Health Organization. Middle East respiratory syndrome coronavirus (MERS-CoV). Available at: http://www.who.int/emergencies/mers-cov/en/ (accessed 14 July 2017).
4. Arabi YM, Arifi AA, Balkhy HH, *et al.* Clinical course and outcomes of critically ill patients with Middle East respiratory syndrome coronavirus infection. *Ann. Intern. Med.* 2014; **160**; 389–397.

5. Cha RH, Joh JS, Jeong I, *et al.* Renal complications and their prognosis in Korean patients with Middle East respiratory syndrome-coronavirus from the central MERS-CoV designated hospital. *J. Korean Med. Sci.* 2015; **30**; 1807–1814.

6. Eckerle I, Müller MA, Kallies S, *et al. In-vitro* renal epithelial cell infection reveals a viral kidney tropism as a potential mechanism for acute renal failure during Middle East Respiratory Syndrome (MERS) coronavirus infection. *Virol. J.* 2013; **23**; 359.

7. Ng DL, Al Hosani F, Keating MK, *et al.* Clinicopathologic, immunohistochemical, and ultrastructural findings of a fatal case of Middle East respiratory syndrome coronavirus infection in the United Arab Emirates, April 2014. *Am. J. Pathol.* 2016; **186**; 652–658.

8. de Wit E, Rasmussen AL, Falzarano D, *et al.* Middle East respiratory syndrome coronavirus (MERS-CoV) causes transient lower respiratory tract infection in rhesus macaques. *Proc. Natl Acad. Sci. USA* 2013; **110**; 16598–16603.

9. Raj VS, Mou H, Smits SL, *et al.* Dipeptidyl peptidase 4 is a functional receptor for the emerging human coronavirus-EMC. *Nature* 2013; **495**; 251–254.

10. Li K, Wohlford-Lenane C, Perlman S, *et al.* Middle East respiratory syndrome coronavirus causes multiple organ damage and lethal disease in mice transgenic for human dipeptidyl peptidase 4. *J. Infect. Dis.* 2016; **213**; 712–722.

11. Guery B, Poissy J, el Mansouf L, *et al.*; MERS-CoV study group. Clinical features and viral diagnosis of two cases of infection with Middle East Respiratory Syndrome coronavirus: a report of nosocomial transmission. *Lancet* 2013; **381**; 2265–2272.

12. Joshi RM. Middle East respiratory syndrome coronavirus (MERSCoV): perceptions, predictions, preventions and the pilgrimage. *J. Clin. Microbiol.* 2013; **2**; e113.

13. Yeung ML, Yao Y, Jia L, *et al.* MERS coronavirus induces apoptosis in kidney and lung by upregulating Smad7 and FGF2. *Nat. Microbiol.* 2016; **1**; 16004. Article number 16004.

14. Cha RH, Yang SH, Moon KC, *et al.* A case report of a Middle East respiratory syndrome survivor with kidney biopsy results. *J. Korean Med. Sci.* 2016; **31**; 635–640.

15. Leung TW, Wong KS, Hui AC, *et al.* Myopathic changes associated with severe acute respiratory syndrome: a postmortem case series. *Arch. Neurol.* 2005; **62**; 1113–1117.

16. Farcas GA, Poutanen SM, Mazzulli T, *et al.* Fatal severe acute respiratory syndrome is associated with multiorgan involvement by coronavirus. *J. Infect. Dis.* 2005; **191**; 193–197.

17. Gu J, Korteweg C. Pathology and pathogenesis of severe acute respiratory syndrome. *Am. J. Pathol.* 2007; **170**; 1136–1147.

18. Chau TN, Lee KC, Yao H, *et al.* SARS-associated viral hepatitis caused by a novel coronavirus: report of three cases. *Hepatology* 2004; **39**; 302–310.